Continuum Mech. Thermodyn. (2019) 31:691–702
https://doi.org/10.1007/s00161-018-0720-0

ORIGINAL ARTICLE

Jonas von Kobylinski · Robert Lawitzki · Michael Hofmann · Christian Krempaszky · Ewald Werner

Micromechanical behaviour of Ni-based superalloys close to the yield point: a comparative study between neutron diffraction on different polycrystalline microstructures and crystal plasticity finite element modelling

Received: 24 August 2018 / Accepted: 19 September 2018 / Published online: 12 October 2018

Abstract To investigate the microstructure-dependent relationships in polycrystalline Ni-based superalloys (Haynes 282 and Inconel 718) deformed in the elastoplastic regime, the lattice strain evolution along various macroscopic directions and along various crystallographic directions is monitored via in situ neutron diffraction during uniaxial tensile loading. In addition, a crystal plasticity-based finite element model is set up to describe the micromechanical behaviour of a unit cell within a uniaxially loaded polycrystalline aggregate. Appropriate postprocessing of the (micromechanical) field quantities allows to simulate the diffraction experiment and thus to directly compare and to discuss experimental and modelling results.

Keywords Neutron diffraction · Crystal plasticity · Nickel-based superalloy · In situ tension test

1 Introduction

1.1 Motivation

Ni-based superalloys are known for retaining significant resistance to loading under static and creep conditions up to high temperatures and are therefore utilized in gas turbines. A widely employed Ni-based superalloy is Inconel 718, which is hardened by precipitation of the ordered γ'- and γ''-phases. A previous study on Inconel 718 [1] revealed a dependence of micromechanical and macromechanical behaviours during plastic loading experiments of the respective microstructure, which was varied by different heat treatments. Mechanical behaviour on the microscale is of technical relevance, as it influences the bulk macroscopic mechanical behaviour and influences the diffraction-based residual strain analyses being important for component lifetime estimates. Haynes 282 is a γ'-precipitate hardened Ni-based superalloy combining creep performance with resistance to strain-age cracking [2]. Qualitative differences between the lattice strain evolutions within Haynes

Communicated by Andreas Öchsner.

J. von Kobylinski (✉) · C. Krempaszky · E. Werner
Institute of Materials Science and Mechanics of Materials, Technical University of Munich, Boltzmannstr. 15, 85748 Garching, Germany
E-mail: woste@wkm.mw.tum.de

R. Lawitzki
Institute of Materials Science, Chair of Materials Physics, University of Stuttgart, Heisenbergstr. 3, 70569 Stuttgart, Germany

M. Hofmann
Research Neutron Source Heinz Maier-Leibnitz (FRM II), Technical University of Munich, Lichtenbergstr. 1, 85748 Garching, Germany

282 and Inconel 718 observed during loading experiments [3] raised the question of whether or not different micromechanical effects are present. Beyond dislocation slip on the octahedral slip systems, many further plastic deformation mechanisms are known to exist for Ni-based superalloys, such as dynamic strain ageing, Kear–Wilsdorf lock formation and anomalous yielding. These effects are especially relevant at elevated and high temperatures.

1.2 Comparison to previous studies

In frameworks aiming at modelling plastic deformation experiments on polycrystal specimens, material parameters are estimated (e.g. the elastic constants or parameters describing plastic flow) in order to relate certain features in model predictions (e.g. to describe the linear elastic behaviour or the point where a significant deviation from the linear elastic behaviour is observed for the first time) to measured data. Care must be taken, such that the number of observed features is significantly larger than the number of free microscopic model parameters. Otherwise, there exists potential susceptibility to overdefining the problem: model material parameters $\leftrightarrow$ measured microscopic evidence. When trying to adequately describe the influence of additional phases and additional micromechanical effects, even more material parameters are required, further increasing the need for micromechanical evidence. Complementary single-crystal loading studies, or utilizing previous single-crystal studies as input, are able to alleviate this need for micromechanical information. Diffraction techniques access grain orientations and elastic strain components, while crystal plasticity models grain orientation evolution and mechanical behaviour. This interplay between crystal plasticity and diffraction techniques has been utilized in earlier studies of several authors. The problem of overdefinition can be counteracted by utilizing multiple reflections and sample orientations as is done in [4] (2 orientations, 4 reflections), [5] (2 orientations, 13 or more reflections), [6] (2 orientations, 2 reflections), [7] (2 orientations, 4 reflections), [8] (2 orientations, 4 reflections).

As the focus of this study involves intergranular strain formation and since postmortem analyses yield significant intragranular plastic strains, it became necessary to model the grain–grain interactions with high spatial resolution. This was achieved by producing a 3-D finite element crystal plasticity model with an adequately fine mesh, featuring a large number of elements per grain. To ensure a large amount of independently observed features, in this study, each sample was measured along 5 directions with respect to the loading direction.

1.3 Overview

The paper is organized as follows:

In Sect. 2, the microstructures are discussed in Sect. 2.1, while the neutron diffraction experiments are outlined in Sect. 2.2, where the temperature-dependent phase relations were aimed at, and in Sect. 2.3, where in situ neutron diffraction during tensile loading is described. In Sect. 3, a modelling approach is discussed, starting with the utilized geometry (Sect. 3.1), then the used constitutive laws (Sect. 3.2) and ending with the postprocessing (Sect. 3.3). In Sect. 4, the obtained results are discussed. It begins with a comparison of the behaviours of phases present in Haynes 282 (Sect. 4.1), then discusses the micromechanical behaviour of Haynes 282 and Inconel 718 (Sect. 4.2) together with simulative output and then finally discusses the micromechanical behaviour of these alloys close to the yield point in Sect. 4.3. The paper ends with conclusions presented in Sect. 5.

2 Experimental

Thermal neutron diffraction on polycrystalline (macroscopic) specimens is utilized for studying both the micromechanics during in situ loading and the temperature-dependent phase relations during heating experiments. Due to the electric neutrality of neutrons, they typically interact only weakly with electrons and penetrate deeply into many materials. As the wavelength of thermal neutrons is comparable to typical interatomic distances, they are capable of resolving distances between atomic nuclei within bulk samples. Changes in the lattice spacings can be caused by thermal loading, mechanical loading and chemical shifts, allowing to refer back to such influences by using an appropriate model. The large number of grains within the gauge volumes in neutron diffraction experiments presented here ensures a good grain counting statistics, making the neutron

counting statistics the main error source. The fit errors (from least squares fits utilizing neutron counting statistics) of all diffraction data in this study (e.g. lattice misfits and lattice strains) are indicated as error bars, which are often smaller than the symbols used in the diagrams. Further types of error are discussed in Sect. 4.2.

2.1 Specimens characterization

Haynes 282 samples were solution annealed at 1010 °C for two hours, then water-quenched, machined to round tensile specimens with a diameter of 6 mm, age-hardened at 788 °C for eight hours and air-cooled. Grain sizes determined via electron backscatter microscopy were approx. 22 μm or approx. 11 μm when counting twin boundaries as grain boundaries. Transmission electron microscopy revealed spherical γ' precipitates with size of approx. 25 nm. In addition to γ-matrix and γ'-precipitates, titanium nitride and carbides with high Mo content were also observed with volume fractions below 1%.

Inconel 718 samples were analogously prepared, albeit with an additional age hardening step, according to the material's standard heat treatment: solution annealing at 975 °C for two hours, subsequent air cooling to room temperature, an eight-hour hardening step at 718 °C, with subsequent furnace cooling to 621 °C, where it was held for further eight hours followed by a final air cooling step. Studies based on small-angle neutron scattering and complementary electron microscopy revealed a grain size of $11 \pm 0.5\mu$m, δ-phase precipitates sized $0.9 \pm 0.4\mu$m with a volume fraction of $2.7 \pm 0.1\%$, γ'-phase precipitates sized 6.9 nm with a volume fraction of 3.1 ± 0.4 % and γ''-phase precipitates sized 4.0 nm with a volume fraction of 3.8 ± 0.6 % .

2.2 Coherency strains prior to plastic deformation

For further microstructure characterization of the initial state, diffraction tests were performed on a Haynes 282 specimen at the powder diffraction beamline SPODI [9] at the MLZ utilizing the (551) reflection of a Ge-monochromator, a wavelength of 1.55 Å and an aperture of 15.5 mm × 4 mm in the primary beam. High-resolution neutron diffractograms were acquired at several temperature levels between room temperature and 840 °C, and Rietveld analyses [10] were performed using the `Fullprof` software [11], to evaluate the lattice misfit evolution with rising temperature (see Sect. 4.1 for the discussion of these results).

2.3 Neutron diffraction during tensile loading

In situ neutron diffraction during uniaxial tensile loading was performed on polycrystalline Haynes 282 and Inconel 718 specimens. Like all diffraction techniques performed on polycrystals, neutron diffraction studies lattice spacings and, hence, elastic strain components of those crystallites which are aligned with a representative of a certain family of crystallographic directions along the measurement direction within the respective gauge volume. In the case of multiple crystallites fulfilling these criteria, their respective signals are superimposed. In this uniaxial loading study, the angle between measurement and loading direction was named ι. This naming was chosen in order to contrast a different notation, using Ψ [12] (s. Fig. 1a). The related, but, due to surface sensitivity and small typical gauge volumes, different X-ray diffraction techniques, where Ψ describes the angle between surface normal and measurement direction [13], are expected to yield significantly dissimilar results, especially when focusing on intergranular and interphase strains within coarse-grained materials.

Tests were performed at the STRESS-SPEC instrument at the MLZ utilizing the (311) reflection of a Ge-monochromator and a wavelength of approx. 1.75 Å . This allowed measuring the (111), (200) and (220) reflections of the matrix (with small contributions from the precipitates) while also allowing to measure the pure (100), (110), (210) and (300)/(221) reflections of the γ' precipitate phase. The primary slit aperture size was 5 mm × 5 mm, whereas a radial secondary collimator with a field of view of 5 mm was used, leading to a nominal gauge volume of 5 mm × 5 mm × 5 mm [15]. The samples were installed within a uniaxial tensile load frame, which was mounted on a Eulerian cradle (s. Fig. 1b). In total, 35 deformation states were evaluated for each Haynes 282 specimen and Inconel 718 specimen, respectively, for each of which the above reflections were measured. The selectivity of diffraction can be utilized for comparing the responses of crystallites depending on their orientations with respect to the tensile axis during plastic deformation. As shown in Fig. 2a, in the plastic regime, the lattice strains deviate from a straight line and are known to deviate positively for the (200)- and negatively for the (220)-reflection in Ni-based superalloys [1]. This is commonly interpreted as a load redistribution from (220)-oriented grains to (200)-oriented grains [16]. However, a direct,

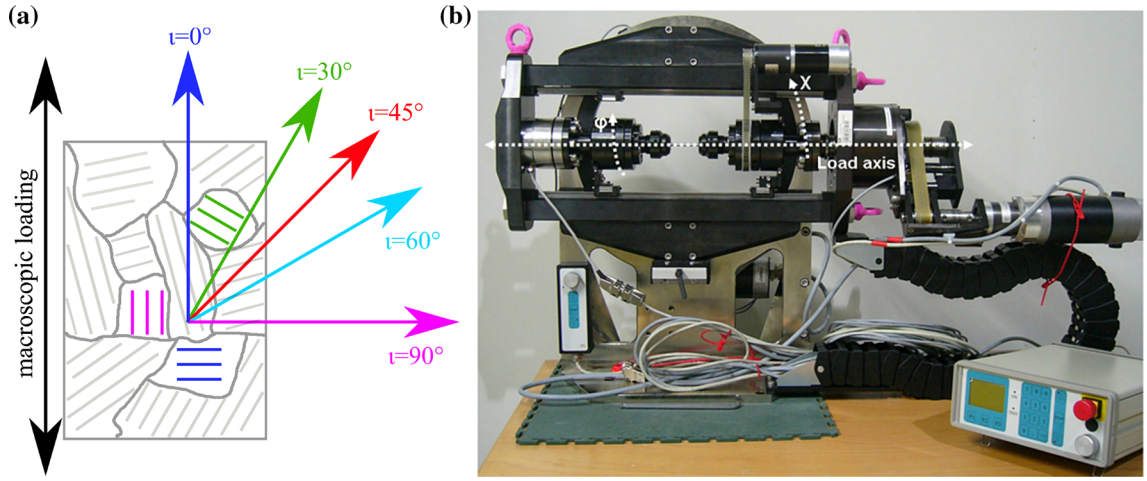

Fig. 1 **a** Image of an exemplary region within a uniaxially loaded specimen. Included are the ι-values for different measurement directions and exemplary grains with corresponding lattice planes contributing to the respective measurements. A further selection in the contributing crystallites is made in their lattice spacings by the choice of reflection. **b** Image of the tensile machine mounted on the Eulerian cradle used in experiments. ι was varied by changing the Eulerian angle $\chi = 180° - \iota$. Picture taken from [14]

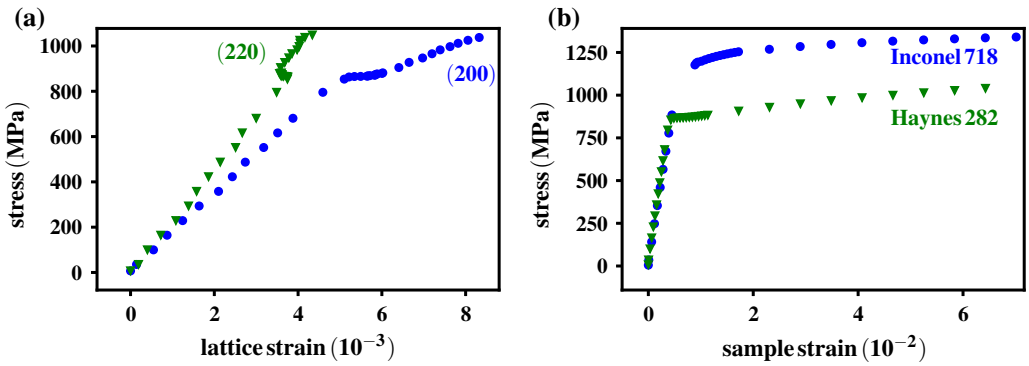

Fig. 2 **a** Sample stress over lattice strain along tensile direction measured from the (200)-reflection (blue circles) and the (220)-reflection (green triangles) within Haynes 282. **b** Macroscopic stress–strain evolutions within Haynes 282 (green triangles) and Inconel 718 (blue circles). Noteworthy are the different shapes of the stress–strain curves after the initial linear regime: sharp for Haynes 282 and rounded for Inconel 718 (color figure online)

quantitative reconstruction of the grain orientation-dependent stress state in a polycrystal is hindered by two facts. Firstly, the vectorial nature of the measured lattice strains contrasts the tensorial nature of the stress states within the measured grains, making any reconstruction of the stress state non-unique. Secondly, the superposition of different crystallites smears out the impacts of various micromechanical effects, e.g. from different crystallites with different shapes, different orientations or different surroundings.

As previous experiments pointed towards further micromechanical effects, in order to gain sufficient micromechanical evidence (see Sect. 1.2), all reflections were measured along 5 directions ι relative to the loading direction: 0° (parallel), 30°, 45°, 60° and 90° (perpendicular). During diffraction studies for each deformation state, the total strain of the sample was held constant. The macroscopic stress–strain curves (s. Fig. 2b) display qualitatively different behaviours in the different shapes of their yield points. (see Sect. 4 for results)

3 Modelling

The experiments performed allow a deep insight into the details of intergranular strain formation by monitoring lattice strain evolutions within crystallites (grains) of different orientation of a polycrystal elastoplastically deformed under macroscopic uniaxial tensile loading. The observations are governed by (elastic and plastic)

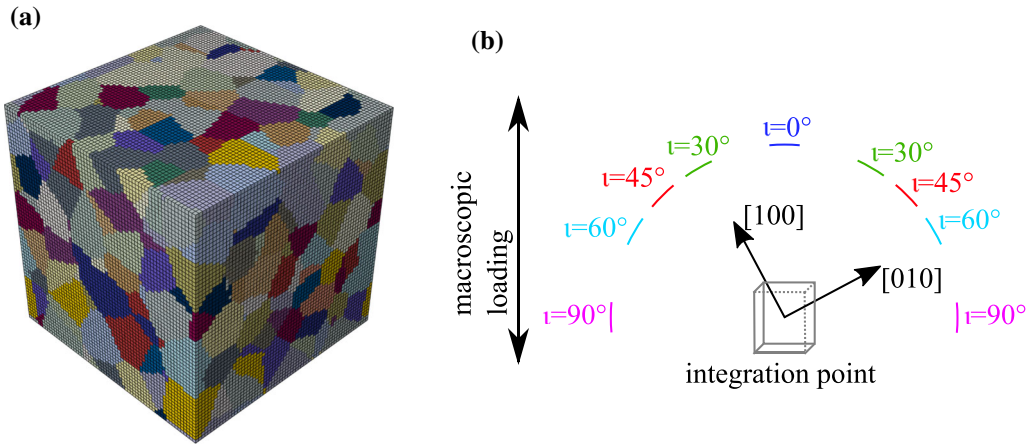

Fig. 3 a The initial state of the unit cell, containing 240 Voronoï-tessellated grains, with approx. 1100 cube shaped elements (C3D8) per grain. The grains are randomly oriented and differently coloured for visualization. **b** The [100]- and the [010]-orientations within an exemplary crystallite region represented by an integration point. Also given are sections through the spherical zones representing the measuring directions. The elastic strain in crystallographic [100]-direction is seen to contribute mainly to the $\iota = 30°$ measuring direction, while the strain in crystallographic [010]-direction contributes mainly to $\iota = 60°$

crystal anisotropy, the activated (crystallographic) mechanisms of plastic deformation, and the interaction of adjacent grains. However, as stated above, a direct, quantitative and complete reconstruction of the grain orientation-dependent strain and stress evolution in the polycrystal from the obtained data is non-unique if not even impossible. To interpret and to discuss the experimental data, a continuum micromechanical model is set up to describe the stress and strain fluctuations in a polycrystalline aggregate on grain level induced by uniaxial loading. Appropriate postprocessing of the simulation results allows a direct comparison to the experimental data. The micromechanical model is implemented into the general-purpose finite element analysis software `Abaqus/Standard`, adopting the software `neper` for Voronoï tessellation and meshing [17,18] and the software `DAMASK` for implementation of the crystal plasticity constitutive model [19–23].

3.1 Model geometry and size

A cubic micromechanical unit cell is constructed containing 240 grains which are generated by Voronoï tessellation on the basis of a periodic random point field. This periodic unit cell is discretized by 64^3 cube shaped elements (element type C3D8) resulting in approx. 1100 elements per grain (s. Fig. 3a). A set of periodic boundary conditions is applied, simulating the response of an infinite three-dimensional array of identical cells containing the virtual grain structure. The unit cell is subjected to uniaxial loading.

3.2 Constitutive equations

To describe the constitutive response on a granular scale, the modular implementation `DAMASK` of the classical continuum crystal plasticity framework based on the multiplicative decomposition of the deformation gradient is applied. In a first approach presented in this contribution, the phenomenological formulation `plastic_phenopowerlaw.f90` is utilized, where the critical resolved shear stress τ^α serves as state variable for each representative α of the octahedral slip systems of the fcc crystal system.

$$\tau^\alpha = \mathbf{S} : \left(\mathbf{m}^\alpha \otimes \mathbf{n}^\alpha\right) \tag{1}$$

$$\dot{\gamma}^\alpha = \dot{\gamma}_0 \left|\frac{\tau^\alpha}{\tau_c^\alpha}\right|^m \operatorname{sgn}\left(\tau^\alpha\right) \tag{2}$$

$$\dot{\tau}_c^\alpha\,(T) = \sum_{\beta=1}^{12} q_{\alpha\beta} \left[h_0 \left(1 - \frac{\tau_c^\beta}{\tau_s}\right)^a\right] \cdot \left|\dot{\gamma}^\beta\right| \tag{3}$$

Here, $\mathbf{m}^\alpha$ and $\mathbf{n}^\alpha$ are the slip direction and the plane normal of the respective slip system, τ^α is the resolved shear stress (analogous to Schmid's law), γ^α is the plastic shear, $\dot{\gamma}_0$ is a reference shear rate, τ_c^α is the critical resolved shear stress, m is a parameter for the rate sensitivity of slip, $q_{\alpha\beta}$ is a measure for latent hardening that accounts for variable cross hardening between different slip systems, and τ_s accounts for the saturation of hardening. h_0 and a are hardening parameters. The elastic constants were chosen from a linear interpolation between the values of γ-Nickel and γ'-Ni_3Al. As for smaller assumed fractions here, the deviations in the elastic regime were larger, the γ' phase volume fraction for calculating the elastic constants was chosen as an upper bound of the volume fraction: 20%. This leads, together with the values for the γ-phase from [24] and the values for the γ'-phase from [25], to $c_{11} = 244.76$ GPa, $c_{12} = 149.22$ GPa and $c_{44} = 123.6$ GPa. These elastic constants relate the elastic strains to the stress state and therefore enter indirectly into the resolved shear stress in Eq. (1). The parameters of the flow rule [Eq. (2)] were chosen to be $m = 20$ and $\dot{\gamma}_0 = 0.001\text{s}^{-1}$. The parameters of the hardening law [Eq. (3)] were chosen as $\tau_s = 393$ MPa, $h_0 = 1000$ GPa and $a = 1.75$, while $q_{\alpha\beta}$ was 1.0 for coplanar slip and 1.4 otherwise [20]. For all unit cell regions, this set of rate equations was initialized with zero plastic shear ($\gamma^\alpha|_{(t=0)} = 0$), and an initial critical resolved shear stress to accommodate the onset of plastic flow ($\tau_c^\alpha|_{(t=0)} = \tau_{c,0} = 187$ MPa).

3.3 Postprocessing

For each deformation state, for all integration points and along all crystallographic directions (within each relevant family of directions), the longitudinal strains were determined. For each pair of these crystallographic directions and measuring directions ι, the intermediate angle was taken and a weighting factor was determined as a centred Gaussian function of this intermediate angle with a standard deviation σ of 7.5°. This continuous and smooth weighting function contrasts the well-defined boundaries of the detector and apertures used in the experiments, but prevents single, rotating grain regions from causing significantly discontinuous predictions. The standard deviation was chosen as a compromise between the angular resolution and the number of strongly contributing crystallites, which is estimated to be critical especially along $\iota = 0°$. Finally, for each family of directions, each measured direction and each deformation state, a weighted average of the longitudinal strains was determined (s. Fig. 3b).

4 Results and discussion

4.1 Phase similarity

Figure 4 shows the lattice misfit evolution with temperature. At approx. 720°C, there is a small, but well-resolved relative increase in the lattice constant of the γ' precipitates with respect to the matrix. Comparison to the simulations of thermodynamic equilibrium [26] indicates the feature at 720°C to stem from an $M_{23}C_6$ to M_6C transition. This is interpreted as a change in the concentrations of carbide forming elements, which influence matrix and precipitates differently, leading to the observed shift in the unstressed lattice spacings. Contrasting this thermodynamic equilibrium study, the μ phase was not present in significant quantities in our

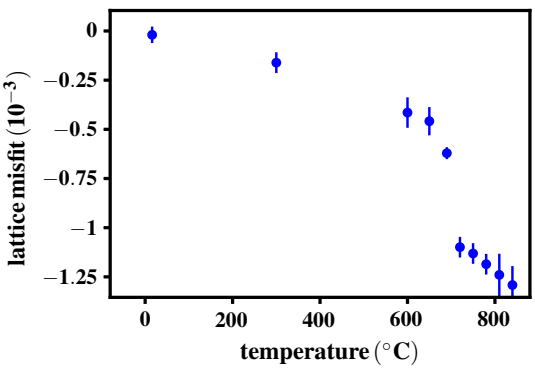

Fig. 4 Lattice misfit evolution with rising temperature within Haynes 282

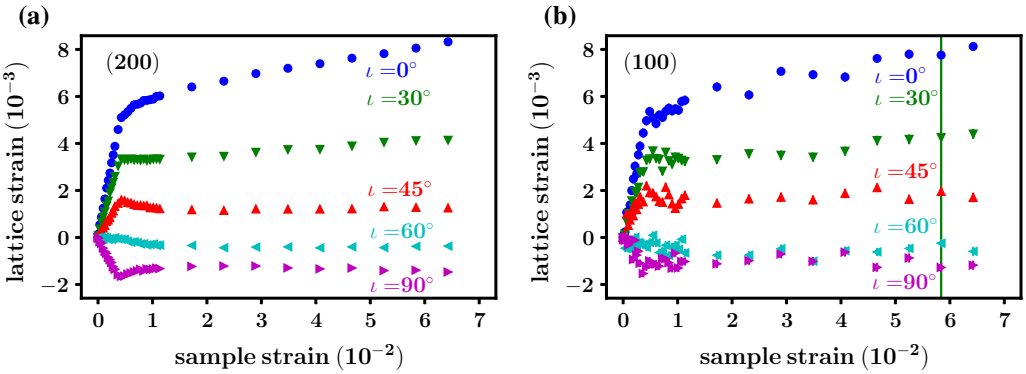

Fig. 5 Lattice strain over sample strain measured from the (200)-reflection **a** and the (100)-reflection **b**. The lattice strains measured from (200) represent the lattice strains of the matrix (with a small contribution from the precipitates), while those measured from (100) result from the precipitate phase

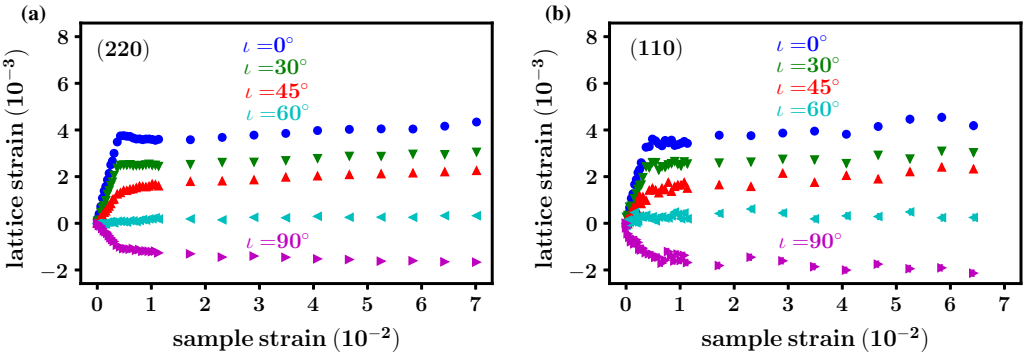

Fig. 6 Lattice strain over sample strain measured from the (220)-reflection **a** and the (110)-reflection **b**. The lattice strains measured from (220) represent the lattice strains of the matrix (with a small contribution from the precipitates), while those measured from (110) result from the pure precipitate phase, only

Haynes 282 specimens. For all temperatures, the lattice misfit remained remarkably small and was negligible at room temperature. This indicates a lack of coherency strains, geometrically necessary dislocations and related stress fields around precipitates at room temperature.

Focusing on intergranular and interphase strain evolution caused by plastic deformation, a sample strain–lattice strain representation was chosen to achieve better comparability. As lattice strains are elastic strain components and the elastic strain tensor is a linear function of the stress tensor, the representation as lattice strain over sample strain along $\iota = 0°$ is closely related to an orientation- and phase-resolved stress–strain diagram. The lattice strain evolutions measured from the crystallographically equivalent (200)- and (100)-reflections are shown in Fig. 5a, b. The (200)-reflection was resolved with a higher resolution than the (100)-reflection, as the γ'-phase volume fraction was only approx. 15%. Both reflections behave very similar to each other, indicating an identical mechanical behaviour of both phases. The lattice strain evolutions measured from the crystallographically equivalent (220)- and (110)-reflections are shown in Fig. 6a, b. Again, both phases display very similar behaviour, which could be resolved for this pair of corresponding reflections with higher resolution than from the previous one.

The lack of load redistribution observable in the nearly identical mechanical behaviours between the γ- and the γ'-phase indicates the inactivity of the Orowan mechanism and the dominance of shearing processes due to the large number density and small size of the γ'-particles [27]. Summarizing, both phases lack stresses with respect to each other before loading, have a very similar crystal structure, are coherent with respect to each other and do not exhibit differences in their mechanical behaviours during loading. This suggests that one can neglect these small differences by treating them both together as one single-phase continuum, as it is done in Sect. 3.

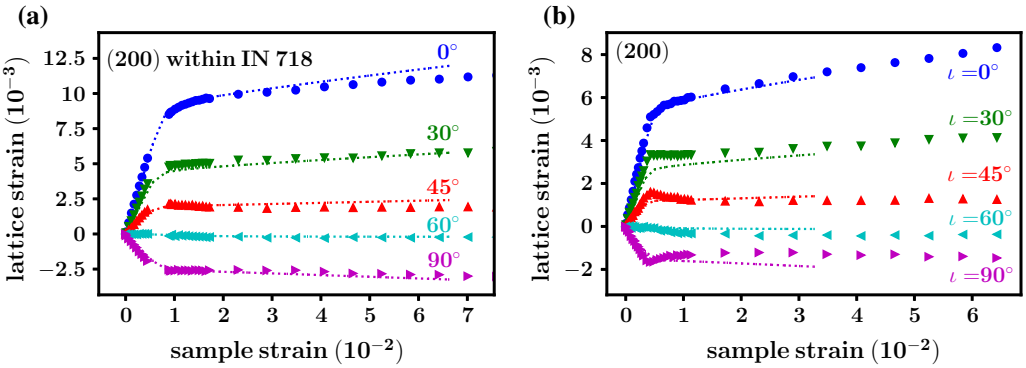

Fig. 7 **a** Inconel 718: measured lattice strain evolution (symbols) and rescaled simulation data (dotted lines) over sample strain obtained from the (200) reflection. **b** Haynes 282: measured lattice strain evolution (symbols) resulting from the (200) reflection and corresponding simulation data (dotted lines) over macroscopic sample strain

4.2 Comparison of diffraction and simulation results

This subsection compares the results of neutron diffraction during tensile loading tests on Haynes 282 and Inconel 718 with corresponding simulation outputs, concentrating on reflections with the highest resolutions: the (200) reflection for Inconel 718 and the (200)-, (111)- and (220)-reflections for Haynes 282. The precipitate reflections have a low resolution due to their low intensities and large widths, whereas the (111) and (220) reflections in Inconel 718 were affected by reflections from different phases.

The measured lattice strain evolutions within Inconel 718 resulting from the (200)-reflection are shown in Fig. 7a along with a rescaled simulation. These simulation outputs were scaled in both sample strains and lattice strains by a factor of 1.65, which was necessary to accommodate the different proportionality limits of Haynes 282 and Inconel 718. For direct comparison between different alloys, the corresponding results from measurements on Haynes 282 are shown in Fig. 7b, along with the corresponding elastic strain components obtained from the same simulation. The lattice strain evolutions within Haynes 282 resulting from the (111)- and the (220)-reflection are shown in Fig. 8 along with the corresponding output from the simulation.

In the elastic regime, the corresponding experimental and predicted curves are in good agreement. The slightly different slopes can be explained by deviations in the anisotropy of the material from the assumed value due to alloying, by the influence of grain size distribution or the influence of twins in the initial state. For Inconel 718, measurement and simulation data are in quite good accordance even in the elastic–plastic regime. However, along the measurement directions $\iota = 45°$ and $\iota = 90°$, deviations between simulation and experimental data with changed monotony behaviour directly after the onset of plastic flow are observed. This type of non-monotonous behaviour is named pronounced microyielding in the following. The pronounced microyielding is even more evidenced for Haynes 282, where it is observed in the same orientations as in Inconel 718 and also along the $\iota = 0°$ measurement direction of (220). Further discussion of the pronounced microyielding is outlined in Sect. 4.3.

The (111)-lattice strain along $\iota = 0°$ is nearly proportional to the uniaxial macroscopic stress. As this behaviour can be beneficial for estimating the macroscopic stress state within polycrystalline specimens by determining their lattice strains and multiplying them with a scaling factor (the diffraction elastic constant), which is frequently utilized for stress measurements. This linear macroscopic stress–lattice strain relation is fulfilled for the simulated (111)-prediction along the tensile axis and is not fulfilled for the other evaluated reflections. The absolute values of the simulated lattice strain evolutions of the (111) reflection are too large in the elastic–plastic transition and in the plastic regimes. When choosing a lower initial critical shear stress, smaller deviations can be expected for this reflection. However, this would also reduce the lattice strains for all other simulation outputs, leading to increasing deviations, for example along the $\iota = 0°$ measurement direction of the (200) reflection. The measured lattice strains, corresponding to the sharp macroscopic yield point, of the (111)-reflection display a sharp transition from the elastic regime to the plastic regime in contrast to the smooth transition of the simulated ones. The absolute values of the simulated lattice strain evolutions of the (220)-reflection of Haynes 282 are overestimated in the elastic–plastic transition and in the plastic regimes for the measurement directions $\iota = 30°$ and $\iota = 90°$.

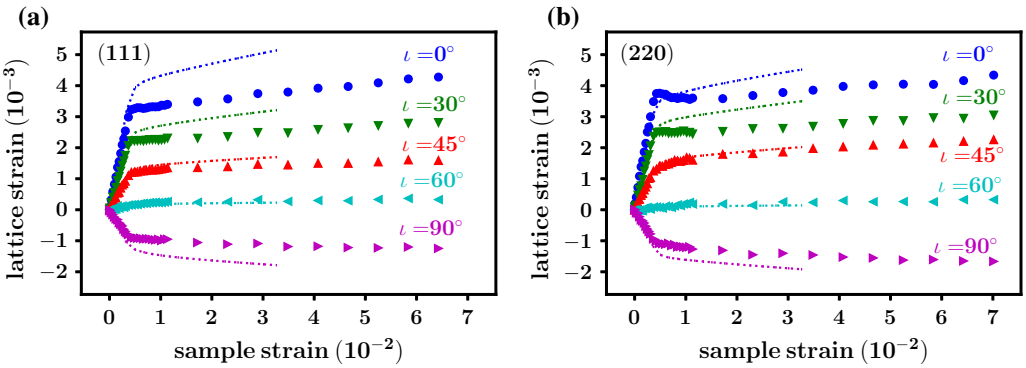

Fig. 8 **a** Haynes 282: measured lattice strain evolution (symbols) and the corresponding simulation data (dotted lines) over sample strain obtained from the (111) reflection. **b** Haynes 282: measured lattice strain evolution (symbols) and the corresponding simulation data (dotted lines) over sample strain obtained from the (220) reflection

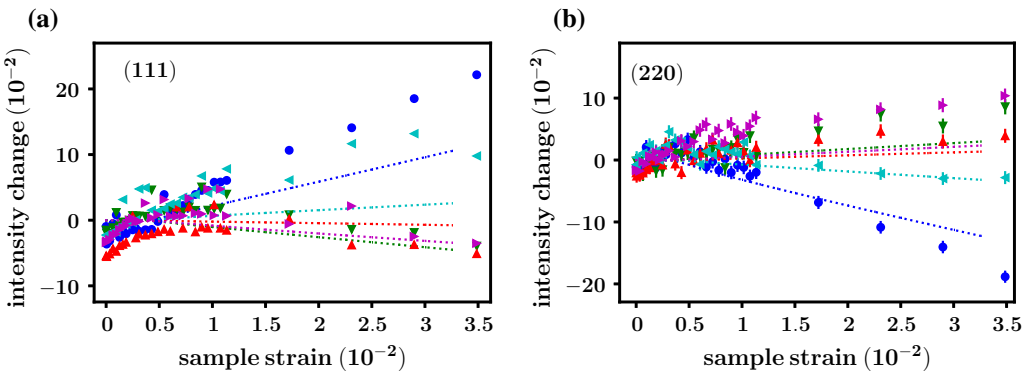

Fig. 9 Relative intensity change over sample strain measured from the (111)-reflection **a** and the (220)-reflection **b** and respective simulated estimates (dotted lines)

As the orientation-dependent weighting in the postprocessing routine results in an intensity change, it can be used to predict the expected effect of texture development on the intensity change. Figure 9a, b shows the measured intensity changes along (111) and (220) together with their simulated estimates. The determination of the intensity changes during measurement was hindered by the unusual beam optics (low mosaicity monochromator and relatively wide apertures), resulting in non-Voigt peak shapes. This can contribute to an erroneous background estimate and thereby contribute to a false determination of intensities. The low solid angle of strongly contributing crystallite orientations induced by the weighting function for the measurement directions $\iota = 0°$ and, to a lesser degree, $\iota = 30°$, leads to a small number of strongly contributing grains. This results in a limited statistics on the grain level and is therefore expected to contribute to deviations here—especially in the intensity evolution.

Due to the large model size, proximity to convergence of the macroscopic behaviour is given, making it a representative volume element with respect to macroscopic behaviour. Yet, the long simulation times (approx. 5.6×10^5 s, utilizing 30 threads on a computer with 80 threads and 40 Intel(R) Xeon(R) CPU E7-8891 CPUs, using approx. 65 GB of cache) and the long postprocessing times (approx. 1.7×10^5 s utilizing a single thread of a hyperthreaded Intel(R) Xeon(R) CPU X5550) make a convergence study in simulated lattice strains or intensity evolutions and an iterative regression in the parameters considered free ($\tau_{c,0}$ and τ_s) of the simulation output to the measured data unfeasible. These studies are, however, not expected to yield qualitatively different results from those presented here, e.g. in the monotony of lattice strain evolution along $\iota = 45°$ and $\iota = 90°$.

4.3 Discussion of pronounced microyielding

Some of the measured lattice strain evolutions showed pronounced microyielding, i.e. a sharp transition from the elastic regime to the plastic regime, followed by continuous softening. This phenomenon may be attributed

to various mechanisms: intergranular residual stresses in the initial state, reduction in the sizes of ordered precipitates due to repeated shearing of precipitates, contribution of additional microscopic deformation mechanisms (e.g. mechanical twin formation), recovery processes during the holding time where the sample strain is kept constant for data acquisition, damage or crack formation and unpinning of dislocations from pinning points (e.g. point defects, segregations, precipitates).

Macro- and microscopic residual stresses in the initial state retained from prior thermomechanical processing may significantly affect the onset of yielding, as shown in a micromechanical study focusing on ferritic–martensitic dual-phase steels [28]. However, the macroscopic initial flow behaviour will be smoothened at the elastic–plastic transition regime contrasting the experimental observations of Haynes 282, where the yield point is sharp.

Repeated shearing of precipitates leads to possible, shortened paths through them and can result in softening [29]. However, this effect is not expected to appear directly at the onset of plastic flow, but rather at significant plastic strain.

Mechanical twinning is capable of spontaneously switching the orientation of crystallite regions, while also causing a load redistribution away from strongly loaded microstructure regions. However, in contrast to our observations relevant plastic deformation by mechanical twinning typically causes significant changes in peak intensity at the yield point and a significant macroscopic work hardening [30].

Recovery processes due to the long times (approximately 9000 s), for which the material was held at constant strain can also produce softening. However, at room temperature, no significant recovery processes are expected for Ni-based superalloys.

The sample is not deformed continuously, but stepwise. Therefore, effects similar to those induced by cyclic loading cannot be entirely ruled out. However, relevant crack growth and formation of pores in ductile specimens in the regime of small plastic strains and very low number of cycles do not seem plausible.

The unpinning of dislocations from pinning points may lead to an unstable transition from the elastic to the plastic regime, characterized by upper and lower yield points (static strain ageing) or to serrations in the macroscopic stress–strain curve (dynamic strain ageing). Typically, Cottrell atmospheres (arrangements of interstitial solute atoms) act as pinning points and lead to strain localization, e.g. Lüders band formation. The observed macroscopic behaviour neither showed strain localization, nor pronounced yielding, nor serrated stress–strain curves, but the shape of the yield point was sharp. However, the observed phenomenon of pronounced microyielding can be interpreted as evidence of unstable plastic flow, taking place in a subset of specially oriented grains. This is in agreement with strain localizations on the microscopic level as slip band formation observed by ex situ electron microscopy.

A rough analysis suggests that the grains mainly contributing to the lattice strain evolutions that show pronounced microyielding belong to the grains where dislocation slip starts: Each ⟨220⟩-oriented grain has four representatives of ⟨200⟩ orientations towards $\iota = 45°$ and two ⟨200⟩ representatives oriented towards $\iota = 90°$. Hence, the pronounced microyielding at $\iota = 0°$ observed for the ⟨220⟩-oriented grains can be interpreted as the onset of flow happening first for these grains, leading to their softening, while the same feature can be observed in $\iota = 45°$ and $\iota = 90°$ on the (200) reflection.

The low concentrations of carbon within the presently studied materials and the large expected fraction of carbon bound within carbide phases suggest the observed pronounced microyielding not solely to be caused by interstitial solute atom clouds. Previous studies by different authors focusing on micromechanical effects during plastic deformation at high temperatures within Ni-based superalloys and related materials found the pinning of dislocations not mainly to be caused by interstitial solute atoms, but by segregations of substitutional atoms to dislocations and related planar defects. In a study [31] on creep deformation in single-phase Co–Ni-based specimen, serrated flow and abnormal strain rate dependence on the flow stress in this system, Mo segregations to stacking faults within dissociated dislocations were observed. In a study [32] focusing on creep strength and γ'-precipitate shearing resistance, in an equiatomic Co–Ni-based specimen with γ'-phase hardened γ-matrix, Co, Cr and W segregations to superlattice intrinsic stacking faults were observed. A study [33] on the effects during creep deformation in a γ'-phase hardened Ni-based single-crystal superalloy specimen with γ-matrix observed Cr, Co and Mo segregations to planar faults. This was interpreted as γ-stabilizers segregating to dislocations due to the local γ-order introduced by their stacking faults.

The most plausible explanation for pronounced microyielding in the present study is dislocation pinning by segregations, albeit with strongly suppressed diffusion. In our specimens, pronounced microyielding is more present in Haynes 282 than in Inconel 718. This may result from five facts: first, by the higher Co and Mo concentrations of Haynes 282 promoting segregations of these elements; second, by the larger volume fraction of γ'-phase within Haynes 282 and the potentially different behaviours between segregations in

different ordered precipitates; third, by different precipitate sizes and heat treatment temperatures, leading to different diffusion path lengths and associated required times and influencing diffusion of γ-stabilizers through precipitates; fourth, by the unknown dislocation densities in the initial states and their unknown impact; and fifth, by the interplay between pinning by segregations and further mechanisms hindering dislocation slip, which are evidenced to be different by the different yield limits being higher in Inconel 718.

5 Conclusions

Neutron diffraction during uniaxial tensile loading in the elastic–plastic regime was performed on two polycrystalline Ni-based superalloys, displaying significantly different characteristics of their lattice strain evolutions along five measurement directions. These results provide valuable information about the evolution of intergranular strains during elastic–plastic deformation and their governing mechanisms on the microscopic level. A micromechanical unit cell model utilizing phenomenological crystal plasticity in a finite element framework helps to discuss the diffraction results and allows a direct comparison of the strain evolutions along all measurement directions to the prediction of established theoretical concepts. The results point at relevant and measurable softening mechanisms even at room temperature. This motivates to take into account the phenomena observed here and elsewhere (e.g. slip band formation and pronounced microyielding) in more sophisticated crystal plasticity models. Finally, this study provides further insights on the pinning strengths of segregations to dislocations in bulk polycrystalline Ni-based superalloys and related materials, shedding light on these micromechanical properties in the regime of absent and weak diffusion.

Acknowledgements We gratefully acknowledge the DFG for funding this research within projects KR 3687/3-1, HO 3322/3-1 and WA 3676/1-1. In addition, the authors thank the German neutron source FRM II for providing beam time at instruments STRESS-SPEC and SPODI and the instrument scientist M. Hölzel for his support during and after the powder diffraction measurement.

References

1. Wagner, J., Hofmann, M., Wimpory, R., Krempaszky, C., Stockinger, M.: Microstructure and temperature dependence of intergranular strains on diffractometric macroscopic residual stress analysis. Mater. Sci. Eng. A **618**, 271–279 (2014)
2. Pike, L.: HAYNES® 282™alloy: a new wrought superalloy designed for improved creep strength and fabricability. In: ASME Turbo Expo 2006: Power for Land, Sea, and Air, pp. 1031–1039 (2006)
3. Wagner, J.N., Hofmann, M., Van Petegem, S., Krempaszky, C., Hoelzel, M., Stockinger, M.: Comparison of intergranular strain formation of conventional and newly developed nickel based superalloys. Mater. Sci. Eng. A **662**, 303–307 (2016)
4. Abdolvand, H., Daymond, M.R.: Internal strain and texture development during twinning: comparing neutron diffraction measurements with crystal plasticity finite-element approaches. Acta Mater. **60**, 2240–2248 (2012)
5. Song, X., Zhang, S.Y., Dini, D., Korsunsky, A.M.: Finite element modelling and diffraction measurement of elastic strains during tensile deformation of HCP polycrystals. Comput. Mater. Sci. **44**, 131–137 (2008)
6. Delannay, L., Jacques, P.J., Kalidindi, S.R.: Finite element modeling of crystal plasticity with grains shaped as truncated octahedrons. Int. J. Plast. **22**, 1879–1898 (2006)
7. Woo, W., Em, V., Kim, E.-Y., Han, S., Han, Y., Choi, S.-H.: Stress–strain relationship between ferrite and martensite in a dual-phase steel studied by in situ neutron diffraction and crystal plasticity theories. Acta Mater. **60**, 6972–6981 (2012)
8. Clausen, B., Tomé, C., Brown, D., Agnew, S.: Reorientation and stress relaxation due to twinning: modeling and experimental characterization for Mg. Acta Mater. **56**, 2456–2468 (2008)
9. Hoelzel, M., Senyshyn, A., Juenke, N., Boysen, H., Schmahl, W., Fuess, H.: High-resolution neutron powder diffractometer SPODI at research reactor FRM II. Nucl. Instrum. Methods Phys. Res. Sect. A Accel. Spectrom. Detect. Assoc. Equip. **667**, 32–37 (2012)
10. Rietveld, H.M.: A profile refinement method for nuclear and magnetic structures. J. Appl. Crystallogr. **2**, 65–71 (1969)
11. Rodriguez-Carvajal, J.: FULLPROF: a program for Rietveld refinement and pattern matching analysis. In: Satellite Meeting on Powder Diffraction of the XV Congress of the IUCr, vol. 127 (1990)
12. Howard, C., Kisi, E.: Measurement of single-crystal elastic constants by neutron diffraction from polycrystals. J. Appl. Crystallogr. **32**, 624–633 (1999)
13. He, B.B.: Two-Dimensional X-Ray Diffraction. Wiley, New York (2018)
14. Hoelzel, M., Gan, W., Hofmann, M., Randau, C., Seidl, G., Jüttner, P., Schmahl, W.W.: Rotatable multifunctional load frames for neutron diffractometers at FRM II-design, specifications and applications. Nucl. Instrum. Methods Phys. Res. Sect. A Accel. Spectrom. Detect. Assoc. Equip. **711**, 101–105 (2013)
15. Hutchings, M.T., Withers, P.J., Holden, T.M., Lorentzen, T.: Introduction to the Characterization of Residual Stress by Neutron Diffraction. CRC Press, Boca Raton (2005)
16. Wu, L., Agnew, S., Brown, D., Stoica, G., Clausen, B., Jain, A., Fielden, D., Liaw, P.: Internal stress relaxation and load redistribution during the twinning-detwinning-dominated cyclic deformation of a wrought magnesium alloy, ZK60A. Acta Mater. **56**, 3699–3707 (2008)

17. Quey, R., Dawson, P., Barbe, F.: Large-scale 3D random polycrystals for the finite element method: generation, meshing and remeshing. Comput. Methods Appl. Mech. Eng. **200**, 1729–1745 (2011)
18. Werner, E., Wesenjak, R., Fillafer, A., Meier, F., Krempaszky, C.: Microstructure-based modelling of multiphase materials and complex structures. Contin. Mech. Thermodyn. **28**, 1325–1346 (2016)
19. Roters, F., Eisenlohr, P., Hantcherli, L., Tjahjanto, D.D., Bieler, T.R., Raabe, D.: Overview of constitutive laws, kinematics, homogenization and multiscale methods in crystal plasticity finite-element modeling: theory, experiments, applications. Acta Mater. **58**, 1152–1211 (2010)
20. Roters, F.: Advanced material models for the crystal plasticity finite element method: development of a general CPFEM framework. Technical Report Fachgruppe für Materialwissenschaft und Werkstofftechnik (2011)
21. Roters, F., Eisenlohr, P., Kords, C., Tjahjanto, D., Diehl, M., Raabe, D.: DAMASK: the Düsseldorf advanced material simulation kit for studying crystal plasticity using an FE based or a spectral numerical solver. Proc. IUTAM **3**, 3–10 (2012)
22. Meier, F., Schwarz, C., Werner, E.: Crystal-plasticity based thermo-mechanical modeling of Al-components in integrated circuits. Comput. Mater. Sci. **94**, 122–131 (2014)
23. Roters, F., Diehl, M., Shanthraj, P., Eisenlohr, P., Reuber, C., Wong, S.L., Ma, D., Jia, N., Kok, P.J.J., Fujita, N., Ebrahimi, A., Hochrainer, T., Grilli, N., Janssens, K.G.F., Stricker, M., Weygand, D., Meier, F., Werner, E., Fabritius, H.-O., Nikolov, S., Friák, M., Raabe, D.: DAMASK: the Düsseldorf advanced material simulation Kit for modelling multi-physics crystal plasticity, damage, and thermal phenomena from the single crystal up to the component scale. Comput. Mater. Sci (2018) (**in press**)
24. Kanrar, A., Ghosh, U.: The elastic stiffness coefficients of nickel–iron single-crystal alloys at room temperature. J. Appl. Phys. **52**, 5851–5852 (1981)
25. Wallow, F., Neite, G., Schröer, W., Nembach, E.: Stiffness constants, dislocation line energies, and tensions of Ni3Al and of the γ'-phases of NIMONIC 105 and of NIMONIC PE16. Phys. Status Solidi (a) **99**, 483–490 (1987)
26. Jablonski, P.D., Cowen, C.J., Hawk, J.A.: Effects of Al and Ti on Haynes 282 with fixed gamma prime content. In" Proceedings of the 7th International Symposium on Superalloy 718 and Derivatives, pp 617–628 (2012)
27. Grant, B.M., Francis, E.M., da Fonseca, J.Q., Daymond, M.R., Preuss, M.: Deformation behaviour of an advanced nickel-based superalloy studied by neutron diffraction and electron microscopy. Acta Mater. **60**, 6829–6841 (2012)
28. Fillafer, A., Werner, E., Krempaszky, C.: On phase transformation induced effects controlling the initial flow behavior of ferritic-martensitic dual-phase steels. Mater. Sci. Eng. A **708**, 556–562 (2017)
29. Merrick, H.: The low cycle fatigue of three wrought nickel-base alloys. Metall. Trans. **5**, 891–897 (1974)
30. Bouaziz, O., Guelton, N.: Modelling of TWIP effect on work-hardening. Mater. Sci. Eng. A **319**, 246–249 (2001)
31. Han, G., Jones, I., Smallman, R.: Direct evidence for Suzuki segregation and Cottrell pinning in MP159 superalloy obtained by FEG (S) TEM/EDX. Acta Mater. **51**, 2731–2742 (2003)
32. Titus, M.S., Mottura, A., Viswanathan, G.B., Suzuki, A., Mills, M.J., Pollock, T.M.: High resolution energy dispersive spectroscopy mapping of planar defects in L12-containing co-base superalloys. Acta Mater. **89**, 423–437 (2015)
33. Barba, D., Smith, T., Miao, J., Mills, M., Reed, R.: Segregation-assisted plasticity in Ni-based superalloys. Metall. Mater. Trans. A **49**, 1–13 (2018)